



Enhanced high-temperature oxidation resistance of Mg-Gd-Zn-Zr alloy by YSZ TBC with PEO bond layer



Xuanyi He¹, Yinhua Shao¹, Yichen Li¹, Wei Zhang², Jinlong Wang¹✉, Minghui Chen¹, Shenglong Zhu² & Fuhui Wang¹

Magnesium alloys suffer from significant limitations in high-temperature applications due to poor oxidation resistance, primarily attributed to the non-protective nature of their native MgO scale (Pilling–Bedworth ratio, PBR = 0.81). This study investigates a novel thermal barrier coating (TBC) system, YSZ/PEO/Mg, designed to enhance the high-temperature performance of a Mg-Gd-Zn-Zr alloy. The system consists of an atmospheric plasma sprayed (APS) 8YSZ top coat deposited onto a plasma electrolytic oxidation (PEO) bond layer applied to the Mg substrate. For comparison, a YSZ coating deposited directly on the Mg substrate (YSZ/Mg) was also prepared. Both TBC systems exhibited stability during 100-hour cyclic oxidation at 200 °C. However, under cyclic oxidation at 400 °C for 100 min, the YSZ/Mg coating experienced catastrophic spallation due to interfacial oxidation and thermal stress, exposing the substrate. In contrast, the YSZ/PEO/Mg system maintained excellent integrity. Crucially, a continuous and protective gadolinium oxide (Gd₂O₃) thermally grown oxide (TGO) layer (PBR = 1.29) formed at the Mg/PEO interface during high-temperature exposure. Furthermore, the porous structure of the PEO layer facilitated mechanical interlocking of the YSZ top coat, significantly enhancing interfacial bonding strength. These results demonstrate that the YSZ/PEO/Mg TBC architecture, leveraging the synergistic effects of the PEO bond coat and the protective Gd₂O₃ TGO, provides an effective solution for significantly improving the high-temperature oxidation resistance of magnesium alloys. This approach is particularly promising for demanding applications such as aerospace thermal protection systems.

The exceptional low density of magnesium makes it highly attractive for aerospace lightweighting, offering substantial potential for reducing fuel consumption and increasing payload capacity¹. However, the broader application of magnesium alloys is significantly constrained by inherent material limitations, including a relatively low melting point, high chemical reactivity (particularly with oxygen and moisture), and fundamentally inadequate resistance to elevated temperatures and corrosive environments^{2,3}. These characteristics drive the rapid formation of a native magnesium oxide (MgO) scale upon air exposure, a process that accelerates dramatically at elevated temperatures. Crucially, MgO possesses a Pilling–Bedworth ratio (PBR) of only 0.81, signifying that the volume of oxide formed is less than the volume of metal consumed. This volumetric deficit impedes the formation of a fully coherent and adherent scale. Furthermore, the MgO scale is intrinsically porous and exhibits a non-

protective, typically cubic crystalline structure that fails to act as an effective diffusion barrier³. Overcoming this inherent weakness necessitates the development of advanced strategies specifically designed to enhance the high-temperature oxidation resistance of magnesium alloys for demanding aerospace applications.

Surface modification techniques represent a crucial pathway for mitigating these intrinsic limitations and unlocking the potential of magnesium alloys. A range of methods, including laser surface treatment^{4–6}, chemical conversion coatings^{9–12}, and plasma electrolytic oxidation (PEO)^{13–17}, have been extensively investigated. Laser surface treatment enhances magnesium alloy hardness⁵, wear resistance⁷, and room-temperature corrosion resistance^{4–7}. However, it may suffer from significant drawbacks including high susceptibility to processing defects⁸. Chemical conversion coatings (e.g., chromate, phosphate, or rare-earth

¹Corrosion and Protection Center, Northeastern University, Shenyang, China. ²Institute of Metal Research, Chinese Academy of Sciences, Shenyang, China.

✉ e-mail: wangjinlong@mail.neu.edu.cn

based) offer ease of application and cost-effectiveness but typically provide only barrier protection and may suffer from environmental concerns (e.g., chromates)¹¹, or poor thermal stability at high temperatures due to dehydration¹². Plasma electrolytic oxidation produces harder ceramic-like oxide layers with improved corrosion resistance and bonding strength^{14–17}. However, the primary focus of these studies has largely centered on improving corrosion resistance at ambient or moderately elevated temperatures. Research specifically dedicated to enhancing high-temperature oxidation resistance (typically above 300 °C) using these surface engineering approaches remains comparatively scarce. In this context, Thermal Barrier Coatings (TBCs) emerge as a particularly promising strategy. TBCs are specifically engineered to provide dual functionality: significant thermal insulation to lower the substrate operating temperature and a barrier against oxidizing atmospheres. For instance, Fan et al.¹⁸ fabricated a multi-layered TBC system consisting of an 8 wt.% yttria-stabilized zirconia (8YSZ) top coat and a NiCrAlY bond coat on a magnesium alloy. Their results demonstrated the system's thermal insulation capability: when the coating surface was held at 200 °C, the underlying substrate temperature was significantly reduced to 146 °C. Under sustained thermal loading reaching equilibrium, the substrate stabilized at ~450 °C while the coating surface reached about 530 °C. This substantial temperature gradient directly translates to a marked improvement in the substrate's resistance to high-temperature oxidation.

Despite their demonstrated potential for thermal management and oxidation protection, conventional TBC systems applied to magnesium alloys often suffer from inadequate thermal shock resistance, limiting their long-term durability. A primary driver of this failure is the significant mismatch in the coefficients of thermal expansion (CTE) between the ceramic top coat, metallic bond coats (if used), and the underlying magnesium alloy substrate. This CTE disparity induces substantial cyclic thermal stresses concentrated at critical bond interfaces during repeated heating and cooling cycles. Over time, this stress accumulation can lead to crack initiation and propagation, ultimately resulting in coating delamination and spallation^{19,20}. The problem is particularly acute for magnesium due to its inherently high CTE, generating more severe interfacial stresses than in systems based on lower CTE substrates like nickel superalloys. Research efforts, such as those by Fan^{19,20}, have explored strategies to mitigate this issue, including introducing Ni-P electroplated layers or thermally formed Mg-Al intermetallic diffusion layers as interlayers. While these approaches successfully doubled the thermal shock life compared to baseline systems, the fundamental challenge of achieving optimal interfacial bonding strength persists. Residual stresses and potential weak points at interfaces remain significant concerns for long-term reliability under extended service conditions involving repeated thermal transients.

Surface morphology, particularly roughness, is a well-established factor critically influencing the bonding strength and durability of TBCs, especially those deposited via thermal spray processes like Atmospheric Plasma Spraying (APS), which rely heavily on mechanical interlocking. Eriksson²¹ demonstrated that increasing the surface roughness of the underlying layer (bond coat or substrate) significantly extends the thermal fatigue life of APS-applied TBCs. The rougher surface provides a larger effective bonding area and facilitates superior mechanical keying of the deposited splats. Consequently, an intermediate layer characterized by both high surface roughness and intrinsically strong adhesion to the magnesium substrate holds considerable promise as an effective bond coat for TBC systems. Plasma Electrolytic Oxidation (PEO) treatment inherently produces precisely such a structure on magnesium alloys. The PEO process generates a thick, hard, in-situ grown oxide ceramic coating that is directly integrated with the substrate metal. This coating exhibits a characteristic bi-layer structure: a relatively dense and adherent inner layer adjacent to the substrate, and a more porous outer layer²². Crucially, the coating formation involves complex plasma-chemical reactions at the metal/electrolyte interface, resulting in a coating that is chemically bonded, rather than merely mechanically attached, to the underlying alloy. Furthermore, PEO coatings are renowned for significantly enhancing the substrate's corrosion resistance^{17,23}. These

attributes – strong chemical bonding, inherent corrosion protection, and a rough, porous outer morphology – collectively contribute to PEO coatings exhibiting outstanding adhesion strength to magnesium alloy substrates^{24,25}. These advantages make a PEO layer serving as a bond coat for an APS-deposited 8YSZ top coat a highly viable and effective approach to substantially improve the thermal resistance and durability of magnesium alloys.

Building directly upon this compelling rationale and the demonstrated potential of the PEO/YSZ combination, this study introduces and investigates a novel thermal barrier coating architecture designed for Mg-Gd-Zn-Zr alloys. The core innovation resides in utilizing a plasma electrolytic oxidation (PEO)-generated oxide ceramic layer as the primary bond coat, replacing conventional metallic bond coats (e.g., NiCrAlY) or electroplated interlayers (e.g., Ni-P). This approach fundamentally departs from prior strategies by establishing robust interfacial bonding: the in-situ PEO formation creates a chemically integrated interface with the Mg alloy substrate, transcending mere mechanical adhesion, while its naturally rough and porous outer morphology provides superior mechanical keying and increased surface area for anchoring APS-deposited YSZ splats, significantly enhancing top coat adhesion. Upon this optimized PEO foundation, a conventional 8YSZ top coat is deposited via Atmospheric Plasma Spraying (APS), forming the complete YSZ/PEO/Mg system. To evaluate the performance benefits of the novel PEO bond coat, this research directly compares the YSZ/PEO/Mg system against a conventional 8YSZ coating deposited directly onto the bare Mg-Gd-Zn-Zr alloy substrate (YSZ/Mg). The comprehensive investigation encompasses detailed microstructural characterization of both systems, systematic evaluation of thermal shock lifetime under cyclic heating/quenching, thorough analysis of failure mechanisms causing degradation and spallation, and detailed elucidation of the oxidation resistance mechanism within the YSZ/PEO/Mg system.

Results

Microstructure of as-prepared TBC

Figure 1 presents the fracture cross-sectional morphology of the two coating systems. In the as-prepared state, the interface between YSZ/PEO/Mg-coated and YSZ/Mg-coated samples remains relatively distinct, showing no evident signs of delamination or separation. In Fig. 2a, both the YSZ/PEO and PEO/Mg interfaces exhibit an undulating profile. In contrast, the YSZ/Mg interface in Fig. 2b is predominantly straight. The characteristic morphology of the APS-deposited YSZ layer, featuring microcracks and porosity, is evident in both figures. During the APS process, precursor powder particles are melted and propelled towards the substrate. Upon impact with the cooled substrate surface, these molten droplets undergo rapid solidification, resulting in the formation of a porous and rough coating structure²².

Figure 2 displays the cross-sectional morphology of the as-deposited samples. For the YSZ/PEO/Mg system (Fig. 3a, b), the YSZ top coat is embedded within the porous outer region of the PEO layer. This interlocking structure significantly enhances interfacial bonding strength with the top coat, achieving the intended design objective. Conversely, the YSZ layer deposited directly onto the substrate in the YSZ/Mg sample (Fig. 3c, d) shows a characteristic morphology, including a distinct oxide layer at the interface.

Oxidation behavior of the TBCs

Figure 3 presents the cross-sectional morphology of both coating systems after cyclic oxidation at 200 °C for 100 h. The images demonstrate that the coatings remain well-bonded in both systems. In Fig. 4b, partial penetration of the YSZ into the PEO layer is observed, increasing the interfacial contact area. An oxidized region is visible at the YSZ/substrate interface in Fig. 4d; however, it cannot be determined whether this oxidation occurred during the APS deposition process or the subsequent oxidation experiment.

Figure 4 displays the surface morphology of both samples after cyclic oxidation at 400 °C for 100 min. The coating on the YSZ/PEO/Mg sample (Fig. 5a) maintains its integrity. In contrast, the YSZ layer on the YSZ/Mg sample (Fig. 5b) exhibits partial detachment. EDS analysis (Table 1) shows

Fig. 1 | Fracture microstructures of as-deposited samples under different modes. **a** YSZ/ PEO/ Mg sample under SE mode. **b** YSZ/ PEO/ Mg sample under BSE mode. **c** YSZ/ Mg sample under SE mode. **d** YSZ/ Mg sample under BSE mode.

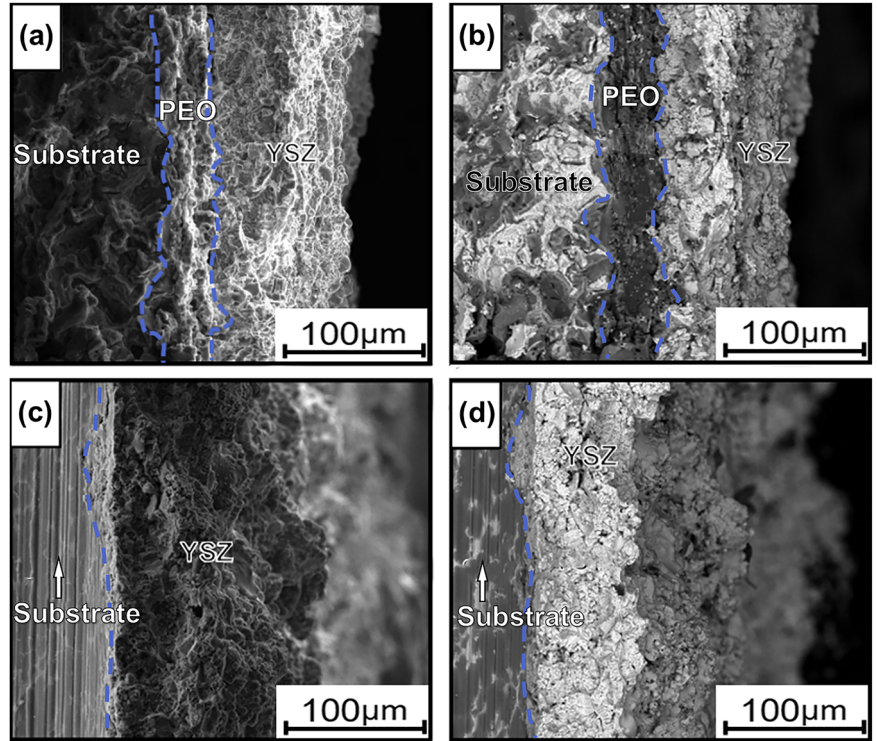
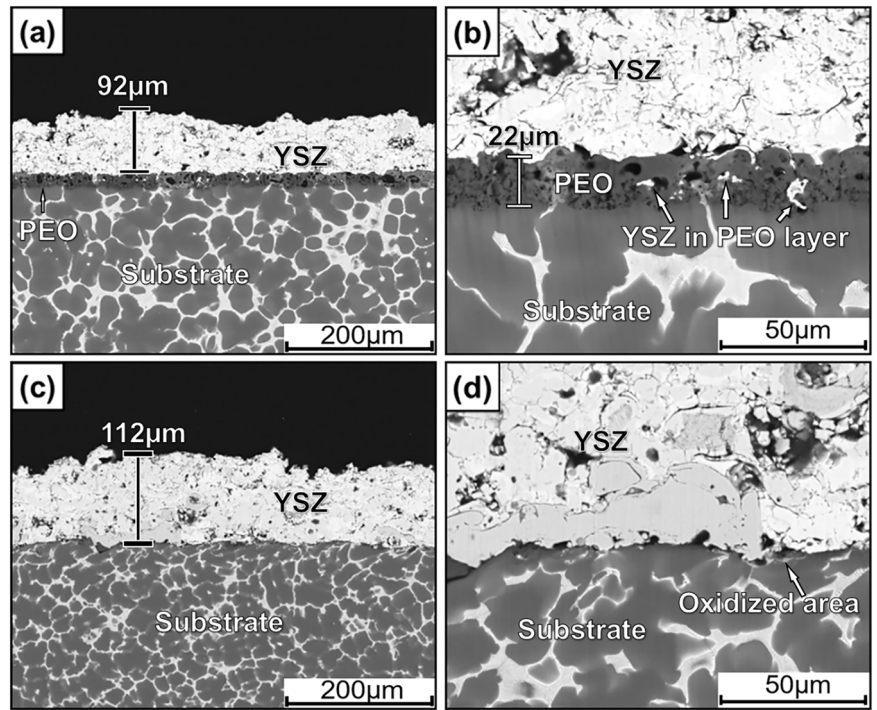


Fig. 2 | Cross-sectional morphologies of the as-deposited samples. **a** Cross-sectional morphology of YSZ/ PEO/ Mg sample. **b** High magnification morphology of (a). **c** Cross-sectional morphology of YSZ/ Mg sample. **d** High magnification morphology of (c).



that Region 1 corresponds to the intact YSZ top coat. In Area 2, however, the atomic percentage of Zr decreased significantly from 20.16% to 4.88%, while the atomic percentage of Mg increased markedly from 1.87% to 34.58%. This compositional shift indicates that the YSZ coating in Area 2 has spalled, exposing the underlying magnesium alloy substrate. These results demonstrate that samples lacking a bond coat cannot provide stable protection at this temperature.

Figure 5 shows the cross-sectional morphology of both systems after cyclic oxidation at 400 °C for 100 min. For the YSZ/PEO/Mg sample (Fig.

6a, b), the interfaces remain well-bonded. A thin, continuous, bright-contrast band is evident at the Mg/PEO interface. The composition and phase identity of this band were analyzed. In the YSZ/Mg sample (Fig. 6c), catastrophic spallation of the YSZ layer has occurred. Within the separation area (Fig. 6d), an oxidized region containing discontinuous thermally grown oxide (TGO) is visible on the Mg substrate. This spallation is inferred to result primarily from thermal stress induced by the mismatch in coefficients of thermal expansion [24]. The oxidation occurring at the interface further weakened the bonding strength.

Fig. 3 | Cross-sectional morphologies of YSZ/PEO/ Mg and YSZ/ Mg samples after cyclical oxidation at 200 °C for 100 h. **a** Cross-sectional morphology of YSZ/ PEO/ Mg sample. **b** The high magnification morphology of (a). **c** Cross-sectional morphology of YSZ/ Mg sample. **d** The high magnification morphology of (c).

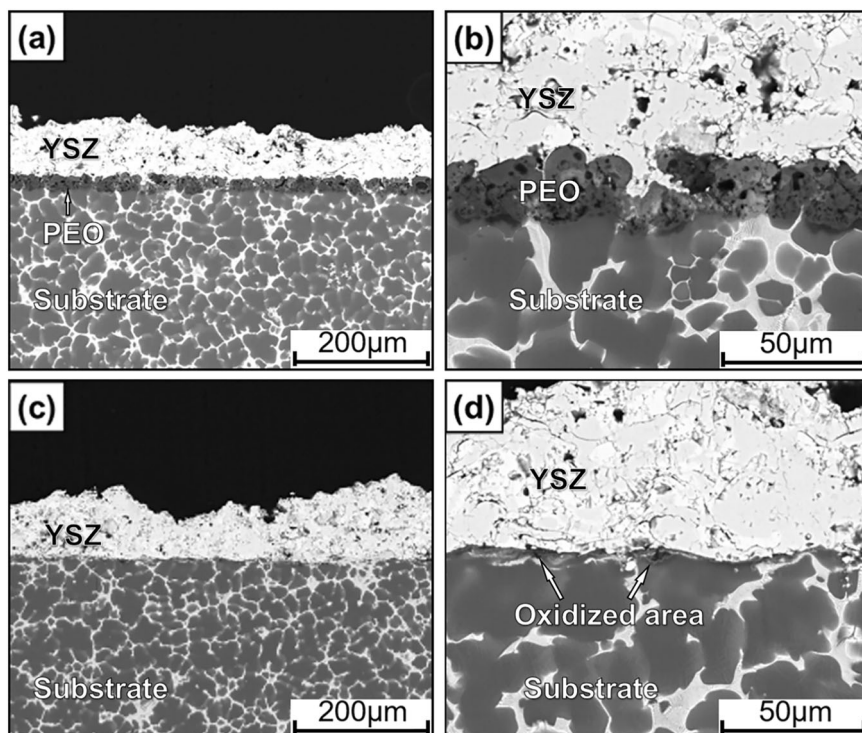


Fig. 4 | Surface morphologies of YSZ/PEO/Mg and YSZ/Mg samples after cyclical oxidation at 400 °C for 100 min. **a** Surface morphology of YSZ/PEO/Mg sample. **b** Surface morphology of YSZ/ Mg sample.

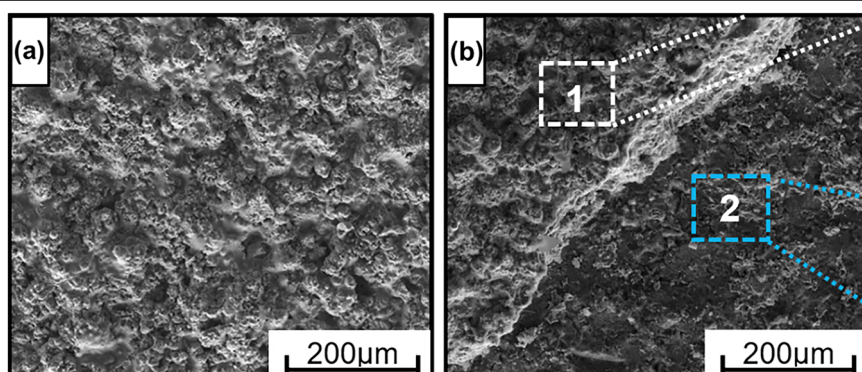


Figure 6 presents TEM micrographs and diffraction patterns of the PEO/Mg interface. Elemental mapping indicates that Gd is predominantly concentrated within the region demarcated by the yellow dashed line. While the presence and distribution of O, Si, Mg, and other elements in this region are less distinct, analysis confirms Gd enrichment within this bright-contrast band. Analysis of the diffraction patterns identifies the phase of the bright-contrast band as Gd_2O_3 . Therefore, it is concluded that this thin band corresponds to a Gd_2O_3 TGO layer formed at the interface between the substrate and the PEO layer.

Figure 7 shows the YSZ/PEO interface morphology of the YSZ/PEO/Mg sample after cyclic oxidation at 400 °C for 100 min. The micrograph indicates that the interface remains well-bonded with no observable inter-diffusion zone or significant degradation.

Discussion

Air Plasma Spray (APS) operates by generating an ultra-high-temperature plasma jet (>10,000 °C) within an atmospheric environment^{26,27}. An electric arc ionizes inert gases (e.g., Ar/H₂) to form this plasma, which simultaneously melts refractory feedstock powders and accelerates the molten droplets toward the substrate. Upon high-velocity impact, the superheated

particles rapidly flatten, solidify, and stack into a dense, lamellar coating capable of withstanding extreme thermal environments. After the APS process, the substrate of Mg/YSZ sample is slightly oxidized in Fig. 3d. When the YSZ particles impact the Mg substrate surface while still in their liquid state, they can cause oxidation of the underlying magnesium. There is no heat affected layer on the substrate. Nevertheless, the oxidized area has negative effect on the bonding strength of the interface. The PEO layer consists of MgO and magnesium silicate^{28,29}, which confirmed by EDS in Fig. 7. The magnesium alloy substrate generates discharge sparks under high voltage, which react in situ in the substrate, undergo diffusion bonding and chemical bonding, and exhibit good bonding strength³⁰. Multilayer structure of PEO layer reported by Guo²⁸ can not be observed clearly in this study. The porous structure provides a channel for YSZ penetrating into PEO layer which can be observed in Fig. 3b. This structure of YSZ embedded in the PEO layer has a bigger bonding strength than YSZ layer on the bare Mg substrate due to the increased contact area.

The susceptibility of magnesium to oxidation during coating deposition and service remains a key concern affecting long-term performance. Therefore, assessing the protective nature of any formed oxide scales is crucial for understanding and mitigating this issue. The Pilling–Bedworth

Fig. 5 | Cross-sectional morphologies of YSZ/PEO/Mg and YSZ/Mg samples after cyclical oxidation at 400 °C for 100 min. a Cross-sectional morphology of YSZ/PEO/Mg sample. **b** The high magnification morphology of (a). **c** Cross-sectional morphology of YSZ/ Mg sample. **d** The high magnification morphology of (c).

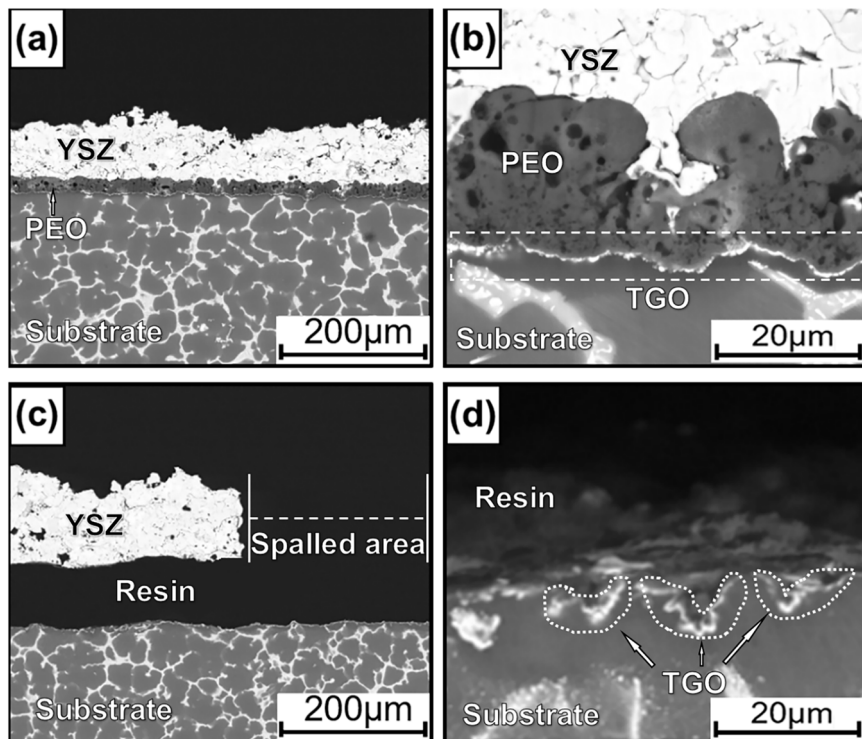


Table 1 | EDS results of “1” and “2” in Fig. 4b (at%)

| Components | O | Mg | Zr | Y |
|------------|-------|-------|-------|------|
| “1” | 76.51 | 1.8 | 20.16 | 1.46 |
| “2” | 57.83 | 34.58 | 4.88 | 0.74 |

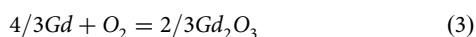
Ratio (PBR) provides a critical criterion for this assessment of the protective integrity of an oxide scale. It is defined as the ratio of the volume of oxide formed to the volume of metal consumed during oxidation:

$$PBR = \frac{V_{oxi}}{V_m} = \frac{M_{oxi}\rho_m}{aA_m\rho_{oxi}} \quad (1)$$

where ρ denotes density, *oxi* refers to the oxide, and *m* refers to the metal. A PBR less than 1 indicates insufficient oxide volume to fully cover the metal surface, while a PBR exceeding 2 typically leads to excessive compressive stresses within the oxide film, promoting spallation. Consequently, a protective and adherent oxide film generally exhibits a PBR between 1 and 2. For pure magnesium, the densities of Mg and MgO are 1.74 g/cm³ and 3.58 g/cm³, respectively³. The resulting PBR of MgO is calculated as 0.81, confirming its inability to form a protective oxide scale.

While no significant morphological changes were observed in either TBC system after oxidation at 200 °C for 100 h, catastrophic spallation of the YSZ layer occurred on the YSZ/Mg sample after exposure at 400 °C for 100 min. In contrast, the PEO/YSZ sample demonstrated superior thermal resistance. Figure 6b reveals the formation of a continuous Gd₂O₃ thermally grown oxide (TGO) layer at the interface between the Mg substrate and the PEO layer.

The oxidation of the Mg substrate involves the following equilibria:



Substituting thermodynamic parameters³¹ at 400 °C yields:

$$\Delta G_{MgO} = -1057.6KJ/mol \quad (4)$$

$$\Delta G_{Gd_2O_3} = -1084.9KJ/mol \quad (5)$$

Figure 8 schematically illustrates the oxidation mechanisms of the two coating systems. As the YSZ layer is an oxygen ion conductor, oxygen readily diffuses through it towards the YSZ/Mg interface. In the YSZ/Mg system, both MgO and Gd₂O₃ can form simultaneously at the interface during the initial oxidation stage, driven by their negative Gibbs free energies of formation. However, the significant thermal expansion coefficient mismatch between the YSZ layer and the magnesium alloy substrate leads to rapid spallation of the YSZ coating. At this stage, only discontinuous Gd₂O₃ form on the exposed Mg alloy surface. Studies indicate that such Gd-containing systems can develop a protective bilayer oxide structure during prolonged oxidation: an outer MgO layer overlying a continuous inner Gd₂O₃ layer³². This continuous Gd₂O₃ layer ultimately functions as an effective protective barrier.

In the YSZ/PEO/Mg system, the initial oxidation process is modified. Although oxygen (O) can still diffuse externally through the YSZ layer towards the YSZ/PEO interface, it must subsequently permeate the PEO layer to reach the magnesium alloy substrate. The presence of pre-existing MgO within the PEO layer effectively simulates oxidation occurring on an Mg alloy already coated with MgO. Consequently, the oxygen partial pressure established at the PEO/Mg interface is dictated by the Mg/MgO redox equilibrium, reaching a relatively high, thermodynamically fixed value, as described by Wagner’s theory. Crucially, Gd₂O₃ possesses a lower (more negative) standard Gibbs free energy of formation compared to MgO. This thermodynamic stability translates to a significantly lower equilibrium oxygen partial pressure required for Gd₂O₃ formation than for MgO formation. Therefore, within the region beneath the PEO layer and adjacent to the Mg substrate – where the local oxygen partial pressure is inherently low – the formation of Gd₂O₃ is thermodynamically favored over MgO.

This preferential oxidation drives the growth of a continuous, dense, and adherent Gd₂O₃ layer, forming a protective thermally

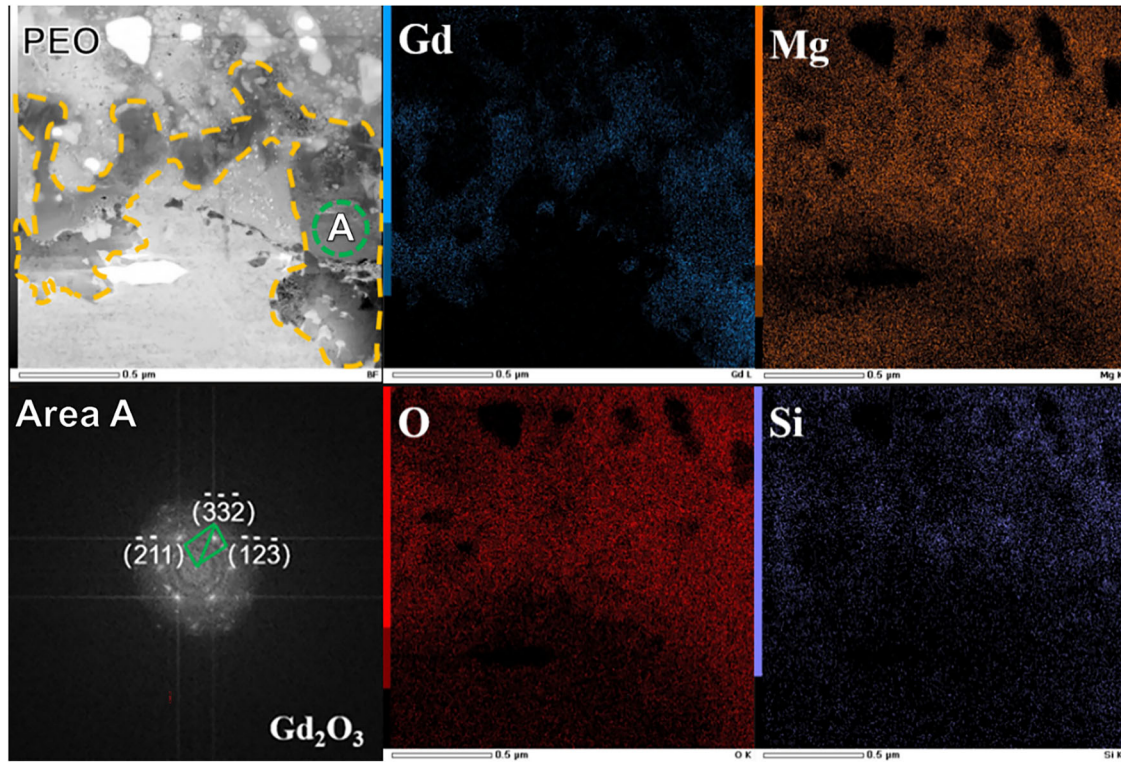


Fig. 6 | Cross-sectional TEM Characterization of TGO in YSZ/ PEO/ Mg sample.

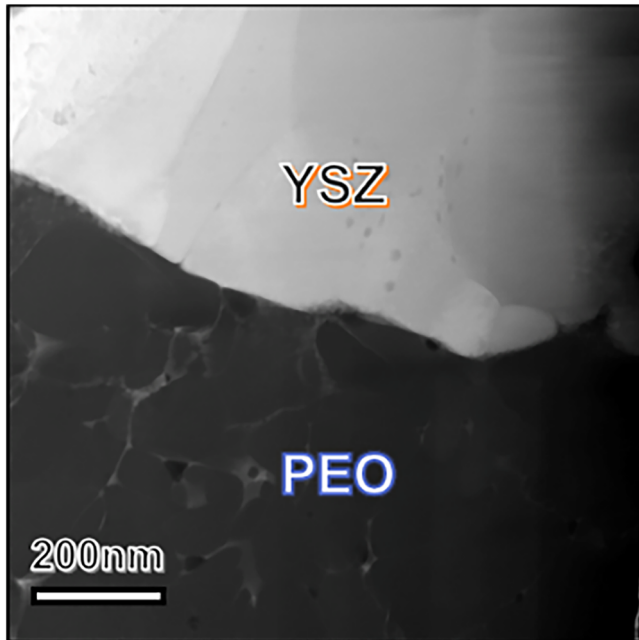


Fig. 7 | Interface morphology of YSZ and PEO of YSZ/ PEO/Mg sample after cyclical oxidation at 400 °C for 100 min by TEM.

grown oxide (TGO) barrier. This effective Gd_2O_3 TGO layer significantly impedes both the inward diffusion of oxygen anions (O^{2-}) and the outward diffusion of magnesium cations (Mg^{2+}). Consequently, the YSZ/PEO/Mg coating system exhibits markedly superior oxidation resistance compared to a YSZ coating deposited directly onto magnesium (YSZ/Mg). Gd_2O_3 exhibits significant oxygen anion conductivity but presents a substantial barrier to cation diffusion³³. Consequently, in the later stages of oxidation, the diffusion rate of O^{2-}

anions through the oxide scale becomes the rate-controlling step. As oxidation continues, the Gd_2O_3 layer, with its favorable PBR of 1.29, develops into a continuous, dense, and protective oxide barrier on the substrate.

Above all, the YSZ/PEO/Mg thermal barrier coating system, constructed by introducing a plasma electrolytic oxidation (PEO) interlayer on the magnesium alloy substrate, significantly enhances high-temperature oxidation resistance. The core mechanism lies in: the unique porous structure of the PEO layer facilitates mechanical interlocking of the YSZ coating, substantially enhancing interfacial bonding strength; more importantly, during high-temperature oxidation, the gadolinium (Gd) element in the substrate undergoes selective oxidation at the PEO layer/magnesium matrix interface, forming a continuous and dense Gd_2O_3 thermally grown oxide (TGO) layer with an ideal Pilling–Bedworth ratio (PBR = 1.29). Future work requires a focused and in-depth investigation into the long-term evolution behavior of the Gd_2O_3 barrier layer, systematic optimization of PEO process parameters to precisely control the continuity of the TGO layer and the interfacial bonding state, and assessment of the evolutionary shift in oxidation kinetics following gadolinium element depletion. The main conclusions are as follows:

- (1) The results demonstrate that both the YSZ/Mg and YSZ/PEO/Mg coating systems maintain stability during 100 h of exposure at 200 °C.
- (2) Following oxidation at 400 °C for 100 min, the YSZ/Mg sample exhibited extensive coating spallation. In contrast, the YSZ/PEO/Mg samples retained significant adhesion to the substrate after the same exposure period, with a Gd_2O_3 thermally grown oxide (TGO) layer identified at the PEO/substrate interface.
- (3) For the novel TBC system developed in this study, the coating maintains robust bonding with the substrate following both long-term low-temperature (200 °C) and high-temperature (400 °C) oxidation. This performance confirms that the YSZ/PEO/Mg structural design is functionally viable and demonstrates excellent cyclic oxidation resistance.

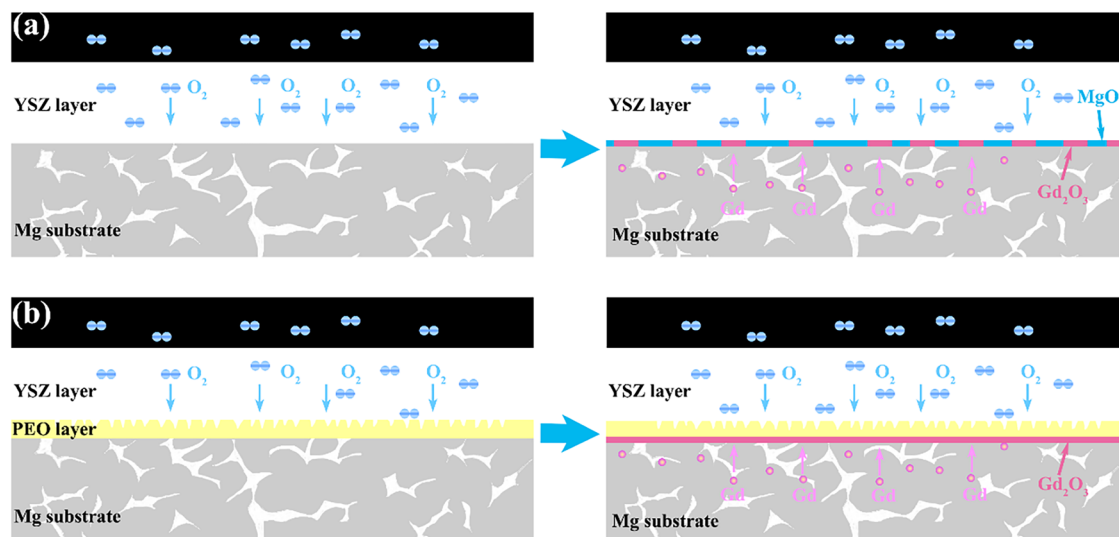


Fig. 8 | Schematic illustration of oxidation mechanisms in a YSZ/Mg and b YSZ/PEO/Mg systems.

Table 2 | Nominal composition of magnesium alloy (wt.%)

| Gd | Zn | Zr | Mg |
|----|-----|----|------|
| 14 | 2.3 | 1 | Bal. |

Table 3 | Electrical parameters and used electrolyte compositions for PEO layer

| Current density | Frequency | Duty ratio | Electrolyte composition |
|---------------------|-----------|------------|--|
| 2 A/dm ² | 1000 Hz | 50% | 5 g/L KF, 2 g/L NaOH, 20 g/L Na ₂ SO ₄ |

Table 4 | Spray parameters for YSZ top coating by APS process

| Argon | Helium | Spray distance | Gun speed | Current | Powder feed rate |
|----------|----------|----------------|-----------|---------|------------------|
| 80 L/min | 50 L/min | 80 mm | 500 mm/s | 900 | 20 g/min |

Methods

Materials

The substrate material used in this study was an Mg-Gd-Zn-Zr alloy (provided by Shanghai Jiao Tong University, Shanghai, China), with a chemical composition as shown in Table 2. The samples had dimensions of 25 mm × 15 mm × 10 mm and were initially ground using SiC abrasive papers to a grit size of 400. Subsequently, they were washed with distilled water and alcohol before being dried in cold air.

The PEO bond coating was manufactured using a plasma electrolytic oxidation system developed by the Institute of Metal Research (IMR). The electrical parameters are shown in Table 3. The alloy samples were subjected to a constant current mode (2 A/dm²) for 15 min to deposit the PEO layer. A cooling system maintained the electrolyte temperature below 30 °C.

Subsequently, the YSZ top coating was prepared using a Metco 7700 plasma spray system (Praxair, USA). Before air plasma spraying, the substrates were grit-blasted to enhance surface roughness and ultrasonically cleaned for 5 min. The Metco 204NS powder (Oerlikon Metco, Westbury, NY) was used to deposit an 8YSZ coating onto both the bare substrate surfaces and the PEO-coated surfaces. The APS parameters are shown in Table 4.

Fracture surfaces for morphological analysis were prepared by cryogenic embrittlement in liquid nitrogen. Samples were immersed in liquid

nitrogen (−196 °C) for a minimum of 10 min to ensure thermal equilibrium, rapidly removed, and immediately fractured using a pre-cooled impact tool. Fractured specimens were promptly transferred to a desiccator to prevent condensation artifacts prior to examination.

Cyclic oxidation

YSZ/PEO/Mg and YSZ/Mg specimens underwent thermal cycling between room temperature and peak temperatures of 200 °C and 400 °C in laboratory air using an automatically controlled circulating heating furnace (ZY-X13, Luoyang Zhongyuan Experimental Electric Furnace Factory, Luoyang, China). For the 200 °C cycle, specimens were heated in the furnace for one hour followed by 10 min of air cooling. For the 400 °C cycle, heating lasted five minutes followed by 10 min of air cooling. Specimens were then removed to examine coating microstructure changes and TGO growth.

Characterization

The phase constituent was characterized by XRD (X’Pert PRO, PANalytic Co., Almelo, Holland, Cu Kα radiation at 40 kV). The obtained X-ray diffraction patterns were recorded in the 2θ range of 10–90°, and a step-scanning mode was employed with a step size of 0.02°. Field-emission scanning electron microscopy (FE-SEM, Inspect F50, FEI Co., Hillsboro, OR, US) coupled with an energy dispersive spectrometer (EDS, X-Max, Oxford instruments Co., Oxford, UK) was used to examine the morphologies and microstructures of the surface and cross-section of the oxidized samples. Transmission electron microscopy (TEM; JEM-2100F, JEOL) coupled with energy-dispersive X-ray spectroscopy (EDS) was employed for detailed analysis.

Data availability

All data included in this study are available upon request by contact with the corresponding author.

Received: 16 July 2025; Accepted: 6 November 2025;

Published online: 02 December 2025

References

- Ishihara, S., Notoya, H., Okada, A., Nan, Z. Y. & Goshima, T. Effect of electroless-Ni-plating on corrosion fatigue behavior of magnesium alloy. *Surf. Coat. Technol.* **202**, 2085–2092 (2008).
- Cui, X. M., Yu, Z. L., Liu, F., Du, Z. X. & Bai, P. C. Influence of secondary phases on crack initiation and propagation during fracture process of as-cast Mg-Al-Zn-Nd alloy. *Mater. Sci. Eng. A* **759**, 708–714 (2019).

3. Song, G. L., Bowles, A. L. & StJohn, D. H. Corrosion resistance of aged die cast magnesium alloy AZ91D. *Mater. Sci. Eng. A* **366**, 74–86 (2004).
4. Gao, Y. L., Wang, C. S., Lin, Q., Liu, H. B. & Yao, M. Broad-beam laser cladding of Al–Si alloy coating on AZ91HP magnesium alloy. *Surf. Coat. Technol.* **201**, 2701–2706 (2006).
5. Khalfaoui, W., Valerio, E., Masse, J. E. & Autric, M. Excimer laser treatment of ZE41 magnesium alloy for corrosion resistance and microhardness improvement. *Opt. Lasers Eng.* **48**, 926–931 (2010).
6. Wang, A. H. & Yue, T. M. YAG laser cladding of an Al–Si alloy onto an Mg/SiC composite for the improvement of corrosion resistance. *Compos. Sci. Technol.* **61**, 1549–1554 (2001).
7. Hong, B. X. et al. Microstructure, wear and corrosion behavior of AZ91D magnesium alloys fabricated by laser surface-modification. *Surf. Coat. Technol.* **498**, 131863 (2025).
8. Liu, S. et al. Influence of laser process parameters on the densification, microstructure, and mechanical properties of a selective laser melted AZ61 magnesium alloy. *J. Alloy. Compd.* **808**, 151160 (2019).
9. Zhang, W. X., He, J. G., Jiang, Z. H., Jiang, Q. & Lian, J. S. Electroless Ni–P layer with a chromium-free pretreatment on AZ91D magnesium alloy. *Surf. Coat. Technol.* **201**, 4594–4600 (2007).
10. Saranya, K., Kalaiyaran, M. & Rajendran, N. Selenium conversion coating on AZ31 Mg alloy: a solution for improved corrosion rate and enhanced bio-adaptability. *Surf. Coat. Technol.* **378**, 124902 (2019).
11. Pommiers, S., Frayret, J., Castetbon, A. & Potin-Gautier, M. Alternative conversion coatings to chromate for the protection of magnesium alloys. *Corros. Sci.* **84**, 135–146 (2014).
12. Lei, L., Shi, J., Wang, X., Liu, D. & Xu, H. G. Microstructure and electrochemical behavior of cerium conversion coating modified with silane agent on magnesium substrates. *Appl. Surf. Sci.* **376**, 161–171 (2016).
13. Saji, V. S. Review of rare-earth-based conversion coatings for magnesium and its alloys. *J. Mater. Res. Technol.* **8**, 5012–5035 (2019).
14. Jiang, B. L. & Ge, Y. F., 7 - Micro-arc oxidation (MAO) to improve the corrosion resistance of magnesium (Mg) alloys. In *Corrosion Prevention of Magnesium Alloys*, 163–196 (Woodhead Publishing, 2013).
15. Li, Z. X. et al. Synergistic effect of hydrophobic film and porous MAO membrane containing alkynol inhibitor for enhanced corrosion resistance of magnesium alloy. *Surf. Coat. Technol.* **357**, 515–525 (2019).
16. Ly, X. N. & Yang, S. Influence of current mode on microstructure and corrosion behavior of micro-arc oxidation (MAO) biodegradable Mg–Zn–Ca alloy in Hank's solution. *Surf. Coat. Technol.* **358**, 331–339 (2019).
17. Zhang, R. F. & Zhang, S. F. Formation of micro-arc oxidation coatings on AZ91HP magnesium alloys. *Corros. Sci.* **51**, 2820–2825 (2009).
18. Fan, X. Z. et al. Preparation and Characterization of 8YSZ Thermal Barrier Coatings on Rare Earth–Magnesium Alloy. *J. Therm. Spray. Technol.* **20**, 948–957 (2011).
19. Fan, X. Z. et al. Improving stability of thermal barrier coatings on magnesium alloy with electroless plated Ni–P interlayer. *Surf. Coat. Technol.* **206**, 4471–4480 (2012).
20. Fan, X. Z. et al. Preparation and Bond Properties of Thermal Barrier Coatings on Mg Alloy with Sprayed Al or Diffused Mg–Al Intermetallic Interlayer. *J. Therm. Spray. Technol.* **23**, 304–316 (2014).
21. Eriksson, R. et al. TBC bond coat–top coat interface roughness: Influence on fatigue life and modelling aspects. *Surf. Coat. Technol.* **236**, 230–238 (2013).
22. Cui, X. J., Ping, J., Zhang, Y. J., Jin, Y. Z. & Zhang, G. A. Structure and properties of newly designed MAO/TiN coating on AZ31B Mg alloy. *Surf. Coat. Technol.* **328**, 319–325 (2017).
23. Chen, C. A. et al. Evaluation of microstructural effects on corrosion behavior of AZ31B magnesium alloy with a MAO coating and electroless Ni–P plating. *J. Mater. Res. Technol.* **9**, 13902–13913 (2020).
24. Fan, X. Z. et al. Preparation and corrosion resistance of MAO/Ni–P composite coat on Mg alloy. *Appl. Surf. Sci.* **277**, 272–280 (2013).
25. Wei, P. X., Chen, L. X., Li, X. R., Gu, H. C. & Chen, D. C. Development of self-healing functional micro-arc oxidation coating on magnesium alloys: a review. *J. Adhes. Sci. Technol.* **38**, 991–1013 (2023).
26. Wei, P., Wei, Z. Y., Zhao, G. X., Bai, Y. & Tan, C. Effect of Processing Parameters on Plasma Jet and In-flight Particles Characters in Supersonic Plasma Spraying. *High. Temp. Mater. Process.* **35**, 775–786 (2016).
27. Padture, N. P., Gell, M. & Jordan, E. H. Thermal barrier coatings for gas-turbine engine applications. *Science* **296**, 280–284 (2002).
28. Guo, H. F., An, M. Z., Huo, H. B., Xu, S. & Wu, L. J. Microstructure characteristic of ceramic coatings fabricated on magnesium alloys by micro-arc oxidation in alkaline silicate solutions. *Appl. Surf. Sci.* **252**, 7911–7916 (2006).
29. Duan, H. P., Yan, C. W. & Wang, F. H. Growth process of plasma electrolytic oxidation films formed on magnesium alloy AZ91D in silicate solution. *Electrochim. Acta* **52**, 5002–5009 (2007).
30. Guo, H. F., An, M. Z., Xu, S. & Huo, H. B. Formation of oxygen bubbles and its influence on current efficiency in micro-arc oxidation process of AZ91D magnesium alloy. *Thin Solid Films* **485**, 53–58 (2005).
31. Dean J. A. 6 – Thermodynamic Properties. In *Lange's Handbook of Chemistry*, 15th ed., 90–115, (McGraw Hill, 2003).
32. Ma, Y. et al. Research on the oxidation behavior of Mg–xGd binary alloys at elevated temperatures. *Mater. Chem. Phys.* **345**, 131287 (2025).
33. Wu, J. J. et al. The oxidation behavior and reaction thermodynamics and kinetics of the Mg–X (X = Ca/Gd/Y) binary alloys. *Corros. Sci.* **225**, 111609 (2023).

Acknowledgements

This project is financially supported by the National Natural Science Foundation of China under Grant (51801021 and 51671053), Fundamental Research Funds for the Central Universities (N25DCG001) and Ministry of Industry and Information Technology Project (MJ-2017–J-99).

Author contributions

X.H.: Conceptualization, methodology, investigation, writing. Y.S. & Y.L.: Investigation. W.Z.: Manufacturing, resources. J.W.: Writing – review & editing, formal analysis, investigation. M.C.: Funding acquisition, resources. S.Z.: resources, supervision. F.W.: supervision.

Competing interests

The authors declare no competing interests.

Additional information

Correspondence and requests for materials should be addressed to Jinlong Wang.

Reprints and permissions information is available at <http://www.nature.com/reprints>

Publisher's note Springer Nature remains neutral with regard to jurisdictional claims in published maps and institutional affiliations.

Open Access This article is licensed under a Creative Commons Attribution-NonCommercial-NoDerivatives 4.0 International License, which permits any non-commercial use, sharing, distribution and reproduction in any medium or format, as long as you give appropriate credit to the original author(s) and the source, provide a link to the Creative Commons licence, and indicate if you modified the licensed material. You do not have permission under this licence to share adapted material derived from this article or parts of it. The images or other third party material in this article are included in the article's Creative Commons licence, unless indicated otherwise in a credit line to the material. If material is not included in the article's Creative Commons licence and your intended use is not permitted by statutory regulation or exceeds the permitted use, you will need to obtain permission directly from the copyright holder. To view a copy of this licence, visit <http://creativecommons.org/licenses/by-nc-nd/4.0/>.

© The Author(s) 2025